Science of Remote Sensing 13 (2026) 100367

Contents lists available at ScienceDirect

Science of Remote Sensing

journal homepage: www.sciencedirect.com/journal/science-of-remote-sensing

Solar-induced chlorophyll fluorescence (SIF) tracks variations in the soil-plant available water (PAW): a multiyear analysis on three crops

Juan Quiros-Vargas [a,*], Cosimo Brogi [b], Alexander Damm [c,d], Bastian Siegmann [a], Patrick Rademske [a], Vicente Burchard-Levine [e], Vera Krieger [f], Marius Schmidt [b], Jan Hanuš [g], Mauricio Martello [h], Lutz Weihermüller [b], Onno Muller [a], Uwe Rascher [a]

[a] *Institute of Bio- and Geosciences, Plant Sciences (IBG-2), Forschungszentrum Jülich GmbH, Jülich, 52428, Germany*
[b] *Agrosphere Institute (IBG-3), Forschungszentrum Jülich GmbH, 52428, Jülich, Germany*
[c] *Department of Geography, University of Zurich, Zurich, CH-8057, Switzerland*
[d] *Eawag, Swiss Federal Institute of Aquatic Science & Technology, Surface Waters – Research and Management, Dübendorf, CH-8600, Switzerland*
[e] *Environmental Remote Sensing and Spectroscopy Laboratory (SpecLab), Spanish National Research Council (CSIC), Madrid, Spain*
[f] *German Aerospace Center (DLR), German Space Agency, 53227, Bonn, Germany*
[g] *Global Change Research Institute of the Czech Academy of Sciences (CzechGlobe), Brno, 603 00, Czech Republic*
[h] *Department of Biosystems Engineering, "Luiz de Queiroz" College of Agriculture (ESALQ), University of São Paulo (USP), Piracicaba, 13418-900, Brazil*

ARTICLE INFO

Keywords:
Fluorescence emission efficiency
Mild water stress assessment
Water management
Airborne imaging spectroscopy
Plant-water relations
Agriculture

ABSTRACT

Restrictions in the soil water availability can strongly impact crop productivity. The increasing frequency and severity of drought events, as a result of global warming, has made the assessment of drought stress effects on vegetation of utmost importance for meeting humanity's agricultural production needs. Recent advances in remote sensing of solar-induced chlorophyll fluorescence (SIF) provide a basis for new approaches to directly assess crop water status, since SIF is closely related to photosynthesis and, thus, to early plant physiological processes triggered by limitations in the water supply. This study provides new insights into the effect of varying levels of plant available water (PAW) in the soil on SIF emissions. We used several SIF datasets acquired with the high-performance airborne imaging spectrometer HyPlant during five subsequent vegetation periods (2018, 2019, 2020, 2021 and 2022), each having a different precipitation regime. We normalized the SIF maps for the underlying effects of canopy structure, calculated SIF emission efficiency (eSIF) and selected various crop fields including sugar beet, wheat and potato. Maps of eSIF were compared with spatial PAW patterns, which were derived from a forward soil infiltration model. Our results show positive correlation between eSIF and PAW in rainfed sugar beet fields at early growing stage, which remained consistent when accounting for variations in the leaf area index (LAI). This suggests that eSIF variations in sugar beet reflect the spatial reduction of photosynthesis caused by reduced PAW. In irrigated potato fields, conversely, no eSIF-PAW correlations were found. This indicates the absence of leaf-level water stress in these well-irrigated fields. In rainfed winter wheat fields that were already in a late developmental stage, the variations in the SIF signal were dominated by locally different ripening, i.e., chlorophyll degradation, and therefore not representative of changing PAW. With this study, we could demonstrate that normalized airborne SIF measurements are related to the functional water stress response in different crops. This study supports future investigations on the development of SIF-based tools for the improvement of water management in agriculture.

1. Introduction

Sensitive and harmonized information in the actual physiological status of crops is essential for the timely detection of water stress, a context where remote sensing emerges as a particularly suited tool. Nevertheless, widely used passive-optical remote sensing approaches based on canopy reflectance and derived vegetation indices tend to represent interwoven biochemical and canopy structural responses, and which are often only sensitive to medium-to long-term water limitation (Damm et al., 2018). Alternatively, thermal remote sensing approaches

---

* Corresponding author.
E-mail address: j.quiros@fz-juelich.de (J. Quiros-Vargas).

https://doi.org/10.1016/j.srs.2026.100367
Received 1 September 2025; Received in revised form 15 December 2025; Accepted 5 January 2026

to estimate canopy temperature can vary due to external factors not related to limitations in water supply, including wind speed, air temperature, and humidity (Gerhards et al., 2019).

Solar-induced chlorophyll fluorescence (SIF) is a low intensity red to far-red light emitted from the photosynthetic apparatus between 600 and 800 nm. The signal is characterized by two emission peaks overlapping two strong atmospheric absorption bands, one in the red and another one in the far-red spectral region, which allows to retrieve SIF at 687 nm (SIF_{Red}) and 760 nm ($SIF_{Far\text{-}red}$), respectively. All the calculations in this study were computed using information from the $SIF_{Far\text{-}red}$, hereafter referred to as SIF (Mohammed et al., 2019; Meroni et al., 2009). Remarkably, the particular sensitivity of SIF to subtle physiological responses to water limitations (Zeng et al., 2022; Mohammadi et al., 2022; Jonard et al., 2020), prior to changes in leaf temperature, leaf orientation (Damm et al., 2018), or pigment degradation (Xu et al., 2018), suggests SIF as an interesting candidate for the early detection of water limitation. Indeed, because of the close relation between SIF and photosynthetic activity (Guanter et al., 2014), SIF has been reported as a suitable complement to reflectance- and thermal-based remote sensing data for the early detection of plant responses to water limitation.

An operational SIF-based water stress assessment has not been established yet, and requires further investigation via combined expertise from various fields, including remote sensing, plant physiology, and soil science. The first fundamental questions to be answered are those related to the spatio-temporal variations of SIF emission in the course of gradually limiting water supply under conventional agricultural field conditions. In this regard, Shen et al. (2021) found SIF information to be more sensitive than the normalized difference vegetation index (NDVI) to changes in surface soil moisture observed at satellite scale (>1 km pixel^{-1}). Yet other studies at satellite scale, e.g., Sun et al. (2015) demonstrated that satellite-observed SIF effectively captured the contrasting drought onset mechanisms in two extreme droughts in North America (in 2011 in Texas and in 2012 in the Great Plains), revealing that SIF can closely track the response of photosynthesis to both prolonged and rapid soil moisture depletion. This evidence was further explored by Mohammadi et al. (2022), who found that a slower than average increase or faster than average decrease, respectively, in the seasonal variation of SIF can be interpreted as an early warning of flash drought events. Furthermore, water stress was found to induce a reduction of vegetation functionality, either via a stronger decrease in the SIF efficiency and gross primary productivity during the afternoon (compared with values recorded in the morning; Zhang et al., 2023), or via a closure of stomata and a reduction of light use efficiency (Wantong et al., 2023). A similar approach based on multi-temporal SIF information using the noon-to-morning ratio to characterize water stress severity was recently proposed by Liu et al. (2023).

At the airborne scale (~1 m pixel size), von Hebel et al. (2018) reported for the first time a significant spatial relation between subsoil apparent electrical conductivity (which can be related to soil physical properties) and canopy SIF of an agricultural field. At a similar scale, Quiros et al. (2020) found a significant spatial match between varying SIF and qualitative soil units, while the commonly used normalized difference vegetation index (NDVI) data appeared homogeneous; a similar pattern was reported by Yoshida et al. (2015), who showed at satellite a higher sensitivity of SIF compared to NDVI in detecting drought-induced reductions in photosynthetic efficiency during the 2010 Russian drought. Subsequently, Damm et al. (2022) assessed the temporal domain and could observe a short-term rise and a subsequent decline of SIF (described as a ‘double SIF response’) to gradually evolving water limitation in high-resolution airborne data. Wang N. et al. (2022), in turn, demonstrated the potential use of UAV-based SIF for water stress assessments at the field level. They observed a significant response of SIF-based indicators during recovery from water stress, whereas only weak responses were detected when drought stress coincided with heat stress. Despite these insights, further studies are necessary to complement existing knowledge on the response of SIF to varying water supply levels in crop canopies.

It is important to note that remote sensing instruments measure only a small part of the total SIF signal that leaves emit in the canopy that is not being reabsorbed by other leaves or scattered out of the instrument's line of sight (Guanter et al., 2014). This escape fraction (f_{esc}) is highly correlated with the structural properties of the canopy rather than leaf physiology (Yang and van der Tol, 2018). Consequently, for a correct physiological interpretation of canopy SIF information, the total SIF signal measured by a remote sensing sensor must undergo a downscaling process to obtain its emission efficiency at the leaf-level (Krämer et al., 2025), hereafter referred to as eSIF. Two methods initially emerged to support this downscaling and are (i) based on the fluorescence correction vegetation index (FCVI; Yang et al., 2020), or (ii) on the near infrared reflectance (NIR) of vegetation index (NIRv; Zeng et al., 2019). Both indices are proxies of f_{esc} that can be derived from remote sensing derived top-of-canopy (TOC) reflectance, and allow normalizing SIF to reduce the canopy structural impact on measured SIF. More recently, Regaieg et al. (2025) introduced a Discrete Anisotropic Radiative Transfer (DART)-based approach that models 3D canopy radiative transfer to separate structural from physiological effects that claims to retrieve photosystem-level fluorescence efficiency. Damm et al., (2022) clearly showed that a throughout normalization of SIF for structural and illumination effects is needed to unravel the SIF inherent sensitivity for evolving water limitation. However, they used a reference area for normalization, which limits the applicability of this approach for larger scale assessments. eSIF-based approaches could overcome this limitation but the sensitivity of such normalized eSIF for evolving water limitation was not investigated yet.

Consequently, we aim to investigate how agricultural environments and conditions couple or decouple the spatial correlation of normalized eSIF and plant available water (PAW) in the soil. We retrieved SIF from airborne based spectroscopy and applied a modified NIRv method (Zeng et al., 2021) to scale canopy SIF to leaf-level SIF (eSIF). We used spatial PAW estimates derived from high resolution (1 m pixel^{-1}) soil data based on hydrogeophysical measurements (i.e., electromagnetic induction; Brogi et al., 2019). The agreement between both datasets was analyzed for five consecutive growing seasons (2018, 2019, 2020, 2021 and 2022) collected over three crop types under different water supply conditions (i.e. irrigated potato, rainfed sugar beet and rainfed winter wheat).

Our investigation was performed in the framework of preparatory studies for the forthcoming FLuorescence EXplorer (FLEX) satellite mission of the European Space Agency (ESA; Drusch et al., 2017), which is planned to be launched in the second half of 2026.

2. Materials and methods

2.1. Study area

The study site was located near the village of Selhausen, western Germany (50.865228° N, 6.450074° E), an agricultural area intensively investigated during the past ten years, and characterized by the cultivation of multiple summer and winter crops (Simmer et al., 2015). We analyzed 15 fields (47.55 ha) covering irrigated potato, rainfed sugar beet and rainfed winter wheat to investigate the influence of contrasting crop and environmental settings (i.e. species, phenology, water supply) on the relationship between eSIF and soil water content. Data were acquired in five years between 2018 and 2022. All investigated fields with their specific surroundings are shown in Fig. 1., while the green dashed line shows the division between an upper and a lower geomorphological terrace shaping the local landscape. The upper terrace has predominantly shallow soils with a fine loess layer (generally up to 30–90 cm depth and locally deeper) covering coarse and compacted sediments. The lower terrace is composed of soil units with a thicker loess layer over a generally less coarse material (Patzold et al., 2008).

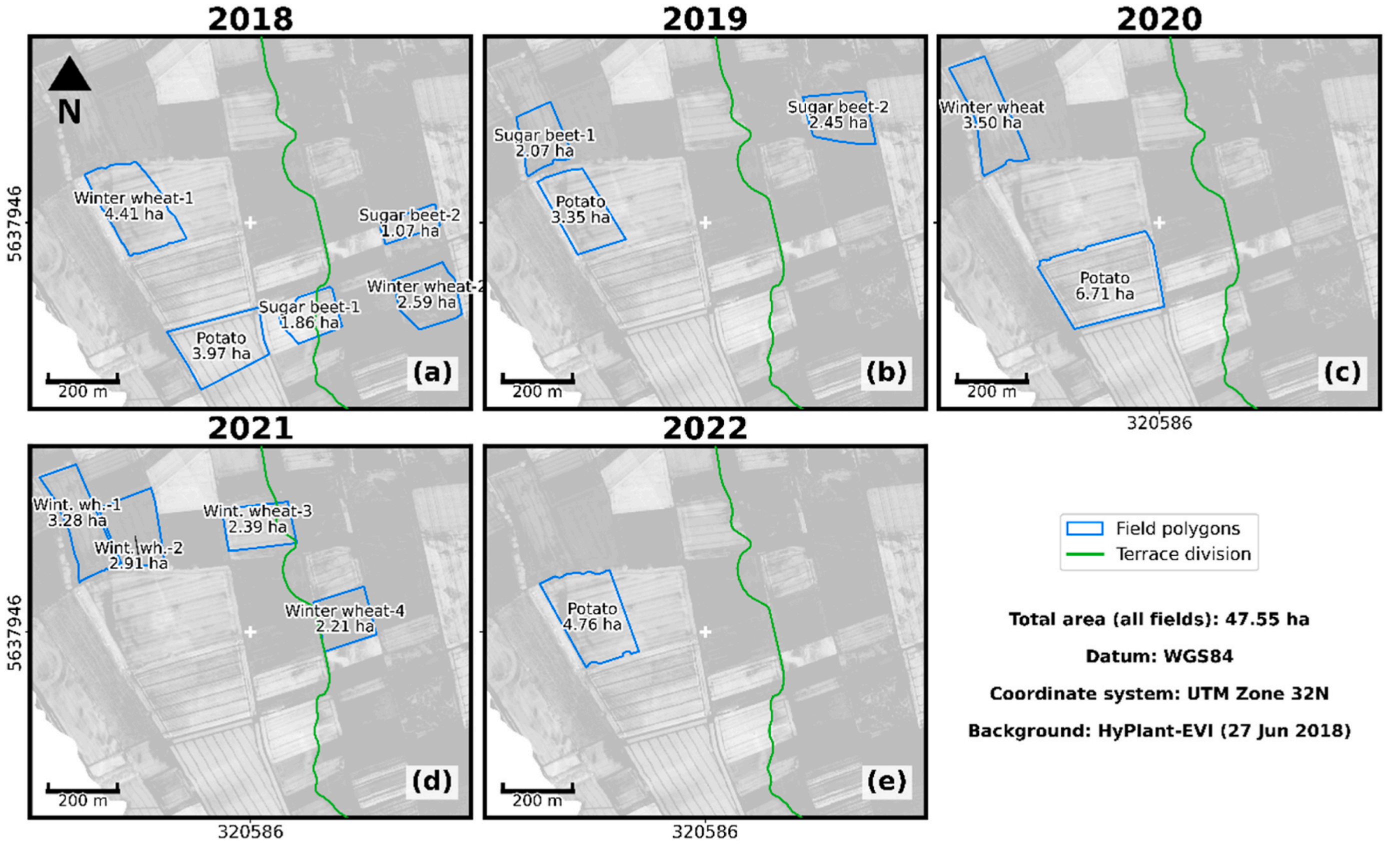

Fig. 1. Location of the studied fields (blue dashed lines) in Selhausen, Germany, in 2018 (June 27th; a), 2019 (June 26th; b), 2020 (June 23rd; c), 2021 (June 13th; d) and 2022 (June 14th; e), with their respective areas (f). Background image: enhanced vegetation index (EVI) computed from high-performance airborne imaging spectrometer (HyPlant) data acquired on June 27, 2018. The green line indicates the border between two landscape shaping terraces. Coordinates system: WGS84, UTM 32N.

2.2. *Remote sensing data acquisition*

Airborne SIF data was acquired over five consecutive growing seasons, i.e., 2018 (June 27th; Figs. 1a), 2019 (June 26th; Figs. 1b), 2020 (June 23rd; Figs. 1c), 2021 (June 13th; Figs. 1d) and 2022 (June 14th; Fig. 1e) in the late morning (~10:30–11:30 h) under cloud-free conditions at 600 m above ground level. During the data acquisition, six flight lines (~360 m width x ~12 km length) were collected using the high-performance airborne imaging spectrometer HyPlant (Siegmann et al., 2019; Rascher et al., 2015). HyPlant is a hyperspectral instrument composed of the DUAL and the FLUO module. The first module measures radiance from 400 to 2500 nm and it is primarily used to compute TOC reflectance and narrow band vegetation indices. The FLUO module was built to enable SIF retrievals, and therefore measures radiance in high spectral resolution at the O_2-A (760 nm) and O_2-B oxygen absorption bands (687 nm) with a full width half maximum (FWHM) of 0.3 nm.

Nano-satellite reflectance imagery from PlanetScope, composed of four spectral bands (i.e., blue (455–515 nm), green (500–590 nm), red (590–670 nm), and near-infrared (780–860 nm)), and atmospherically corrected to the bottom of the atmosphere (Planet Surface Reflectance version 2.0 product), were used to compute enhanced vegetation index (EVI) seasonal curves at high spatial resolution (3 m pixel^{-1}). 24 images (from the sensor Dove Classic – PS2, product Ortho Scene – Analytic 4B SR - Level 3B) were obtained between 2018 and 2022 under cloud-free conditions (Table 1).

2.3. *Remote sensing data processing*

2.3.1. *SIF retrieval*

SIF at a spatial resolution of 1 m was computed for all years (Fig. 3a) using the most recent version of the Spectral Fitting Method (SFM). The SFM method allows the retrieval of SIF and reflectance in adjacent wavelengths over a specific spectral range at both sides of the oxygen absorption bands at 685 and 760 nm (Cogliati et al., 2015). In contrast to other SIF retrieval methods, the SFM algorithm incorporates radiative transfer theory to correct for atmospheric interferences caused by

Table 1
Nano-satellite images obtained from PlanetScope (Planet, 2017), used to estimate the seasonal enhanced vegetation index (EVI) as an approximate reference of crops phenology. DOY stands for “day of the year”. The date is represented in “month.day” format.

Image no.	2018		2019		2020		2021		2022	
	Date	DOY	Date	DOY	Date	DOY	Date	DOY	Date	DOY
1	03.25	84	03.21	80	03.24	84	03.29	88	03.22	81
2	04.18	108	04.20	110	04.15	106	04.27	117	04.23	113
3	05.04	124	05.24	144	05.18	139	05.21	141	05.22	142
4	05.26	146	06.09	160	05.28	149	06.16	167	06.12	163
5	06.27	178	06.23	174	06.20	172	–	–	06.28	179

various factors, including water vapor, aerosols, and surface air pressure. More details about the SFM-based SIF retrieval can be found in Siegmann et al. (2021).

2.3.2. eSIF calculation

We used NIRvH, a modified version of NIRv, which can be calculated from reflectance data. The determination of NIRvH is based on the theory that f_{esc} and the NIR reflectance of vegetation share similar radiative transfer properties (Badgley et al., 2017) and, unlike the FCVI-based approach, accounts for soil background reflectance interference. We specifically used NIRvH2 (Zeng et al., 2021), which is a further development of the original NIRv version and implements a simplified soil background reflectance correction scheme that assumes a linear behavior of soil reflectance in the red-edge spectral range.

We calculated the NIRvH2 from HyPlant DUAL TOC reflectance data according to Zeng et al. (2021) as:

$$\mathrm{NIRvH2} = R_{800} - R_{678} - k^{*}(\lambda_{NIR} - \lambda_{Red}) \tag{1}$$

where, R is TOC reflectance and subscripts represent the spectral windows (in nm), λ_{NIR} and λ_{Red} are set to 800 and 678 nm, respectively. k is the slope of the soil reflectance in the red-edge and was calculated by performing a linear regression on multiple TOC reflectance spectra across the leaf spectral-invariant region (i.e., 778–800 nm) (Fig. 3b). NIRvH2 was subsequently used as a factor in equation (2) to derive the leaf-level SIF emission efficiency (eSIF; Fig. 3c), which accounts for the scattering and reabsorption effects on the SIF signal, and therefore provides information about changes in leaf physiology.

$$eSIF = \frac{\pi^{*}SIF}{iPAR^{*}NIRvH2} \tag{2}$$

iPAR (mW m^{-2}) represents the incoming photosynthetically active radiation obtained from the TERENO climatic station (TERENO, 2022). Since SIF is retrieved from a single angle, it is multiplied by π to approximate the hemispheric SIF emission.

2.3.3. Phenology estimation

Since the SIF emissions are related to crop phenology (Wang X. et al., 2022), we differentiated the investigated crop fields according to their apparent phenological stage. For this, we considered the day of year (DOY) 80–180 to compute the seasonal EVI curves from nano-satellite data, and used EVI as proxy for greenness and biomass. The EVI was selected instead of the more commonly used normalized difference vegetation index (NDVI), since it has been proven to be less affected by saturation in areas with high biomass (Huete et al., 2002). The EVI was computed according to Gao et al. (2000) as:

$$EVI = 2.5^{*}\frac{R_{780-860} - R_{590-670}}{R_{780-860} + 6^{*}R_{590-670} - 7.5^{*}R_{455-515} + 1} \tag{3}$$

Phenology classes were defined based on the time elapsed (Δt) between the HyPlant data acquisition and the start of the season (i.e., for irrigated potato, rainfed sugar beet fields) and peak of the season (i.e., for rainfed winter wheat fields). The start of the season is defined as the time point when the EVI shows a strong increase, whereas the peak of the season is defined as the time point when the EVI starts decreasing. Fields with a start or peak of the season differing by less than five days were considered to be in the same phenology class.

For irrigated potato and rainfed sugar beet, fields with a shorter Δt (<20 days) between the season start and the HyPlant campaign were classified as 'Early phenology', while fields with longer Δt (≥20 days) were considered as 'advanced phenology'. In the specific case of irrigated potato, the advanced phenology fields differed by more than one day in Δt, and therefore were further classified as "Advanced_1", "Advanced_2", and "Advanced_3". For rainfed winter wheat, fields with longer Δt between the season peak and the HyPlant campaign were considered as 'Early phenology', while fields shorter Δt were considered as "advanced phenology".

2.3.4. Leaf area index calculation

The leaf area index (LAI) is considered a sensitive indicator of canopy structural impacts on retrieved SIF (e.g., via scattering and reabsorption). We therefore compared the relationship between SIF and eSIF considering the underlying LAI to assess the actual effect of the downscaling method on retrieved SIF emissions. Therefore, we derived LAI for each pixel from HyPlant DUAL TOC reflectance data using a hybrid approach that combines the capabilities of radiative transfer modeling with machine learning regression techniques (Verrelst et al., 2019). We particularly combined the radiative transfer model PROSAIL (Jacquemoud et al., 2009) with the machine learning technique support vector regression (Smola and Schölkopf, 2004).

2.4. Soil data acquisition

Soil information used in this study have a pixel size of 1 m (i.e., the same as the airborne SIF data) and was derived from geophysics (electromagnetic induction)-based mapping presented by Brogi et al. (2019; Fig. 3d). Brogi et al. (2019) published a ~90 ha soil map of the Selhausen area, which includes the investigated fields and differentiates between 18 soil units that are quantitatively described up to a maximum depth of 2 m. The electromagnetic induction methodology measures apparent electrical conductivity (ECa) at multiple depths of investigation and follows the principle that specific physical properties of a soil will determine its capacity to conduct electricity. Therefore, soil units sharing similar ECa signatures over depth are assumed to share comparable soil characteristics and belong to the same soil class. The geometry of the 18 soil units was determined by analyzing ECa maps using supervised machine learning algorithms, while their specific soil properties were identified with a strategic field sampling directed at 100 representative points. For more information about the methodology, descriptions soil unit's properties, and descriptions soil unit's properties, the reader is referred to Brogi et al. (2019), while Brogi et al. (2020, 2021) have assessed the performance of this map against satellite-based information and in supporting agroecosystem models.

2.5. Soil data processing

2.5.1. Calculation of precipitation regimes

The full PAW capacity ($\mathrm{PAW_{cap}}$) of each soil class has to be corrected according to the specific precipitation regime of each investigated growing season. Therefore, we characterized the precipitation regime of each year via the daily rainfall accumulated during the last 30 days before the HyPlant campaign using rainfall data recorded from the terrestrial environmental observations (TERENO; TERENO, 2022) as:

$$\text{Precipitation regime} = \sum_{i=1}^{30} Daily\ rainfall_{i} \tag{4}$$

The respective accumulated precipitation sums are shown in Fig. 2, indicating 2018 and 2022 as years with higher rainfall (>45 l m^{-2}) and the other years as lower rainfall years with the driest year in 2020. In the years 2019, 2020 and 2021, the accumulated rainfalls were 35.85, 18.00, and 40.40 l m^{-2}, respectively. This information is later used in the study to calibrate the $\mathrm{PAW_{cap}}$ of a soil unit and estimate the actual PAW (hereafter just referred to as PAW) for each year (cf. section 2.6).

2.5.2. Generation of plant available water maps

The Mualem–van Genuchten model (van Genuchten, 1980, Fig. 3e) was used to convert the textural information provided by the geophysics-based soil map into numerical values of $\mathrm{PAW_{cap}}$ (Fig. 3f) as:

$$\theta_w(h) = \theta_r + \frac{\theta_s - \theta_r}{(1 + |\alpha h|^{n})^{m}} \tag{5}$$

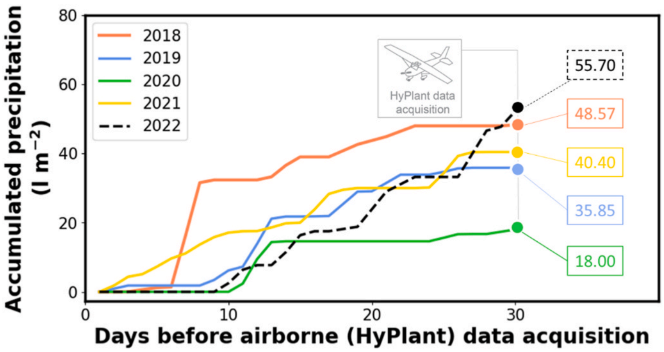

Fig. 2. Cumulative (summed) precipitation during the 30 days prior to high-performance airborne imaging spectrometer (HyPlant) overflights in 2018 (June 27), 2019 (June 26), 2020 (June 23), 2021 (June 13) and 2022 (June 14). Precipitation data were derived from TERENO 2022.

θ_w, θ_r, and θ_s (cm^3 cm^{-3}) are the volumetric, residual, and saturated water content of the soil, respectively. h (kPa) represents the pressure head and α represents the inverse of the air entry pressure (cm^{-1}). The dimensionless n value relates to the distribution of soil pore sizes, and m is a shape parameter related to n by $1–1/n$. The soil hydraulic parameters in eq. (5) were estimated from textural information in the soil map by using pedotransfer functions (PTF). The PTF of Rawls and Brakensiek (1985) with additional corrections for gravel content (Brakensiek and Rawls, 1994) were used as these had previously proven to be effective for this study area (Brogi et al., 2020). The PAW$_{cap}$ was calculated as the difference between the θ_w obtained at $h = -100$ cm (field capacity) and $h = -15000$ cm (wilting point). This calculation was performed on each soil unit of the geophysics-based soil map.

The PAW$_{cap}$ was calculated to a maximum of 2 m soil profile for each crop. Yet, in soil units A1a–d, B1b, D1a–d, and D2, the PAW$_{cap}$ was calculated up to the depth of a compacted coarse layer that is found in those soil units, since it can be assumed that roots cannot penetrate deeply into such compacted coarse material (Daddow and Warrington, 1983).

The PAW$_{cap}$ map, still based on the hydraulic characteristics of each soil unit, was converted to an estimate of the actual PAW (here just referred as PAW) using the accumulated precipitation during the last 30 days prior to the HyPlant data acquisitions (Fig. 2). With this information, we calculated a correction factor (CF), estimating the percentage of the PAW$_{cap}$ filled by the accumulated precipitation. CF's for 2018–2021 were estimated using the rainfall accumulation of 2022 as the reference of the one filling the 100 % of the PAW$_{cap}$ (Fig. 3g). This was done, since 2022 was the year with the highest precipitation recorded the month before airborne SIF data collection. Afterwards, we multiplied the PAW$_{cap}$ map by each year CF to obtain specific year PAW maps (Fig. 3h; an extended version of the materials and methods summary figure, Fig. 3, is presented in Appendix 1).

In the study region, most of the fields are not irrigated and thus PAW$_{cap}$ is mainly determined by natural precipitation. However, potato

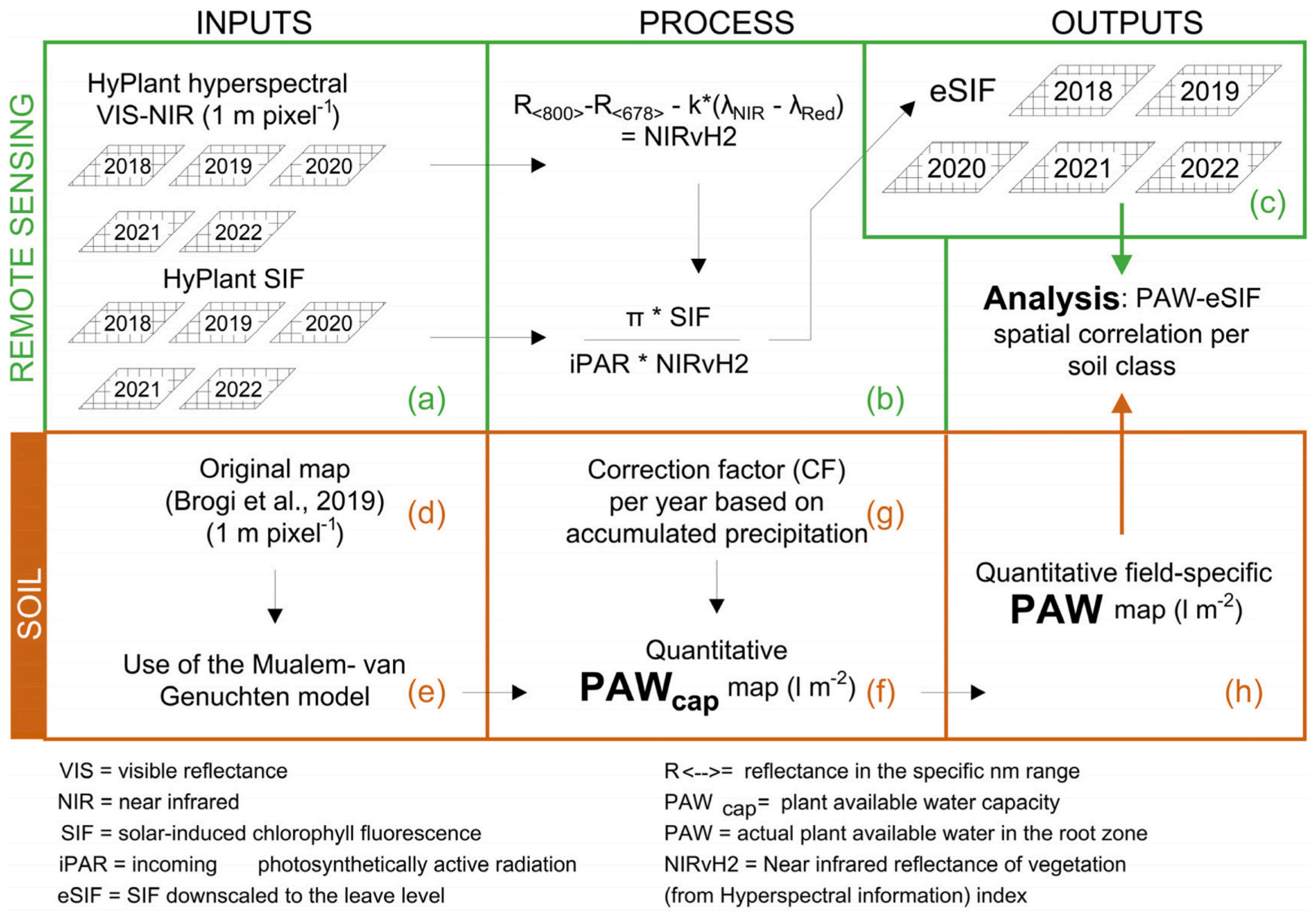

Fig. 3. Summary of materials and methods separated according to inputs, processes, outputs, and analyses implemented with the airborne (a–c) and soil (d–h) datasets. The statistical analysis was done by overlapping the outputs from the remote sensing and soil data processing. All abbreviations are provided at the bottom of the figure. An extended version of this figure is presented in Appendix 1.

fields are irrigated with mobile systems, and therefore, according to standard irrigation practices in the region, 30 l m^{-2} were added to the PAW estimation of those fields. This amount accounts for the water irrigated during the week before the HyPlant data acquisition.

In order to validate our PAW estimates, we analyzed the agreement between PAW_{cap} estimates and time domain reflectometry (TDR)-based soil moisture data (Mengen et al., 2021) measured on June 26, 2019 (the same day of the HyPlant campaign that year). Results are shown on Appendix 2, where 2130 TDR-based volumetric soil water content data from Mengen et al. (2021) are compared against the corresponding PAW_{cap} estimates. A significant ($p < 0.05$) relationship was found between the PAW_{cap} levels and the average TDR-based actual soil moisture. However, it must be noted that this comparison was done only over a region with shallow soils (upper terrace; $PAW_{cap} = 101.42–156.50$ l m^{-2}). Since the soil moisture data measured in the field by Mengen et al. (2021) was representative only for the topsoil (5 cm depth), we considered that the comparisons with deeper soils were not appropriate.

2.6. Data analysis

We aimed to assess the agreement between spatial eSIF dynamics (as dependent variable) and the spatial variation in PAW (as independent variable) considering different environmental and crop settings. In preparation of this analysis, machinery paths were removed from the individual field imagery, since they are not related to the spatial soil water content patterns of interest. Further, polygons (or soil units) smaller than 25 m^2 were removed from the PAW maps.

We investigated the agreement between SIF and eSIF maps from the five study years with the respective field-level PAW maps via overlays. We also calculated the descriptive statistical measures including mean and standard deviation for SIF, eSIF and PAW for each soil unit, and described their agreement via the slope's confidence interval (at 95 % probability), and the Pearson correlation coefficients (r) together with its confidence at 95 % ($p < 0.05$).

A similar analysis was done to compare the SIF and eSIF relations considering LAI dynamics, aiming to understand the effect of the downscaling method. Besides the r and p values, the slope and the mean absolute deviation from the slope-based fit were computed for each SIF- and eSIF-LAI relation. Since SIF and eSIF units present different magnitudes (i.e., SIF ranges between 0 and 4, eSIF between $0\text{-}1\text{x}10^{-4}$), the slopes and the deviations of the SIF- and eSIF-LAI relations were converted to relative values, assuming 3.5 and 1×10^{-4} as 100 %, respectively, yielding relative slope (RS, %) and relative mean deviation (RMD, %) information.

The results of the SIF and eSIF vs. PAW and LAI regressions were differentiated by crop and phenology class. Finally, only pixels with LAI >1 were considered for the study to exclude pixels with low fractional cover and thus with a higher influence from the soil background.

3. Results

The spatial distribution of PAW, SIF, and eSIF are shown for irrigated potato, and rainfed sugar beet and winter wheat over the five growing seasons (Fig. 4). Absolute SIF and eSIF values show large differences between corresponding maps. The highest measured SIF and eSIF values are SIF >2.75 mW m^{-2} nm^{-1} sr^{-1} and eSIF $> 7 \times 10^{-5}$ nm^{-1} and were found in irrigated potato fields, while the lowest SIF <0.5 mW m^{-2} nm^{-1} sr^{-1} and eSIF $< 2 \times 10^{-5}$ nm^{-1} were found in rainfed winter wheat. In general, normalized SIF (eSIF) shows more pronounced spatial patterns compared to SIF. As an example, the paleo river bed patterns in the winter wheat field of 2020 became visible in the eSIF map, while SIF shows a rather homogenous distribution. Such enhancements in the eSIF maps are notable in fields with low to medium SIF emissions, while fields with higher SIF emissions (e.g., potato and sugar beet field 1 in 2018 and potato in 2020) appear similar. Opposite cases can be observed in the irrigated potato fields of 2018 and 2022, where the difference between blue and yellow areas in the eSIF map are less pronounced than those observed in the SIF map.

Despite the above described visual spatial patterns in SIF and eSIF, and the even more contrasting heterogeneity observed in PAW information within and among growing seasons, clear visual spatial correlations are not always obvious between SIF and PAW nor between eSIF and PAW. Thus, a statistical analysis was done to determine the strength of the spatial relation between SIF and eSIF with PAW. Since the analyses focused on data from several years and over different time points within the year (DOY difference of 10 days), we grouped the fields according to their apparent phenological stage.

For irrigated potato (Fig. 5a–d), the 2019 field was at a later phenological stage (Δt of 17 days). For the other years, potato was in a more advanced phenology stage (i.e., “advanced-1” in 2022 with $\Delta t =$ 23 days, “advanced-2” in 2020 with $\Delta t = 26$ days, and “advanced-3” in 2018 with $\Delta t = 32$). All rainfed sugar beet fields (Fig. 5e–h) were considered to be in one unique “early” phenological class, since Δt was 1 day. Rainfed winter wheat in 2018 (Fig. 5i–o) was found to be in an ‘early’ phenological stage (i.e., long Δt of 54 days, while Δt's of 48 and 47 days observed in the 2020 and 2021 indicate winter wheat fields to be in an ‘advanced’ phenological stage.

In Table 2 the Δt between the start and maximum EVI (peak) of the season and the respective HyPlant data collection dates are summarized.

Using the derived phenology classifications, the spatial agreement of SIF and eSIF with PAW for the three different crops was derived by relating the spatial averages of SIF and eSIF per soil unit with a specific PAW level. In irrigated potato fields, regardless of the spatial heterogeneity in PAW, no significant SIF-PAW and eSIF-PAW correlations were found at any of the phenological stages (advanced-1, 2 and 3) (Fig. 6a and d). In rainfed sugar beet fields, both SIF (Fig. 6b) and eSIF (Fig. 6e) significantly ($p < 0.05$) increased with increasing PAW. In rainfed winter wheat fields, no significant correlations were observed at advanced-phenological stages, yet, in the early phenology field, a positive significant relation between SIF and PAW disappeared with the downscaled, eSIF, information (Fig. 6c and f).

We also analyze the effect of normalizing canopy SIF to leaf-level SIF in relation to LAI (Fig. 7, Table 3). All SIF- and eSIF-LAI correlations are significant at $p < 0.05$ (except PO_Advanced_1), and an overall decrease of r and relative slopes can be observed for most eSIF-LAI relationships compared to SIF-LAI relationships (Table 3). This decrease is expected since the normalization intended to reduce the structural impact of LAI on SIF. Also, in all cases the relative residuals in the eSIF-LAI relations showed a notable increase compared to the residuals observed in the SIF-LAI cases. In Fig. 8, a more detailed analysis for rainfed sugar beet fields considering low (LAI 1–3) and high (LAI >3) canopy densities was done, as this case showed the strongest SIF-PAW and eSIF-PAW correlations. In both cases, a significant relation between eSIF and PAW was observed, however, in the low-density canopies (LAI <3) this relation is independent from variations in LAI.

4. Discussion

4.1. Relationship between SIF, eSIF and PAW

We demonstrated that airborne acquired SIF measured at the far-red peak showed a crop species dependent relation to PAW. These dependencies were, however, influenced by LAI and the seasonality of the different crops. Plants have developed multiple strategies to structurally and functionally acclimate to PAW limitations, which are dynamically adjusted to the severity of soil water limitation according to the ecological plasticity of the species. Such strategies, occur at different temporal scales, have a direct impact on the top-of-canopy SIF emission, and include (i) the sensing of water potential by the roots (Dietrich, 2018), (ii) the hormonal (Ramachandran et al., 2020) and hydraulic signaling from the root to the shoot (Christmann et al., 2007), (iii) induced stomata closure (Abdalla et al., 2022), adjustment of root and

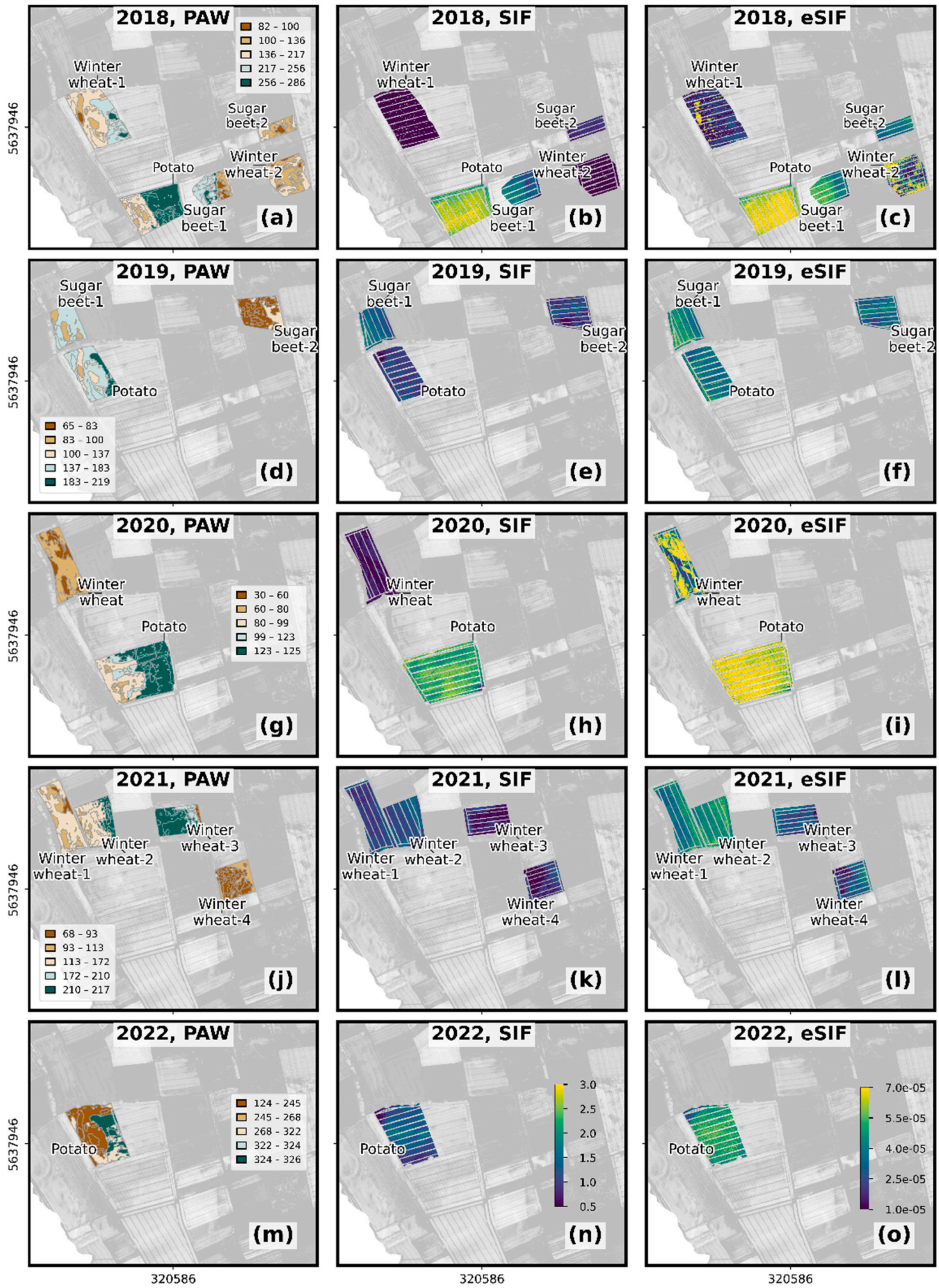

Fig. 4. Plant available water (PAW) maps computed based on the geophysics-based soil map (Brogi et al., 2019) for the fields analyzed in 2018, 2019, 2020, 2021 and 2022 (left column). The solar-induced chlorophyll fluorescence (SIF) and SIF emission at leaf level (eSIF) maps retrieved from the data collected by the high-performance airborne imaging spectrometer HyPlant in 2018 (June 27), 2019 (June 26), 2020 (June 23), 2021 (June 13) and 2022 (June 14) are presented in the center and right column, respectively. Background image: enhanced vegetation index (EVI) derived from HyPlant DUAL top-of-canopy reflectance data recorded on June 27, 2018. Coordinates system: WGS84, UTM 32N.

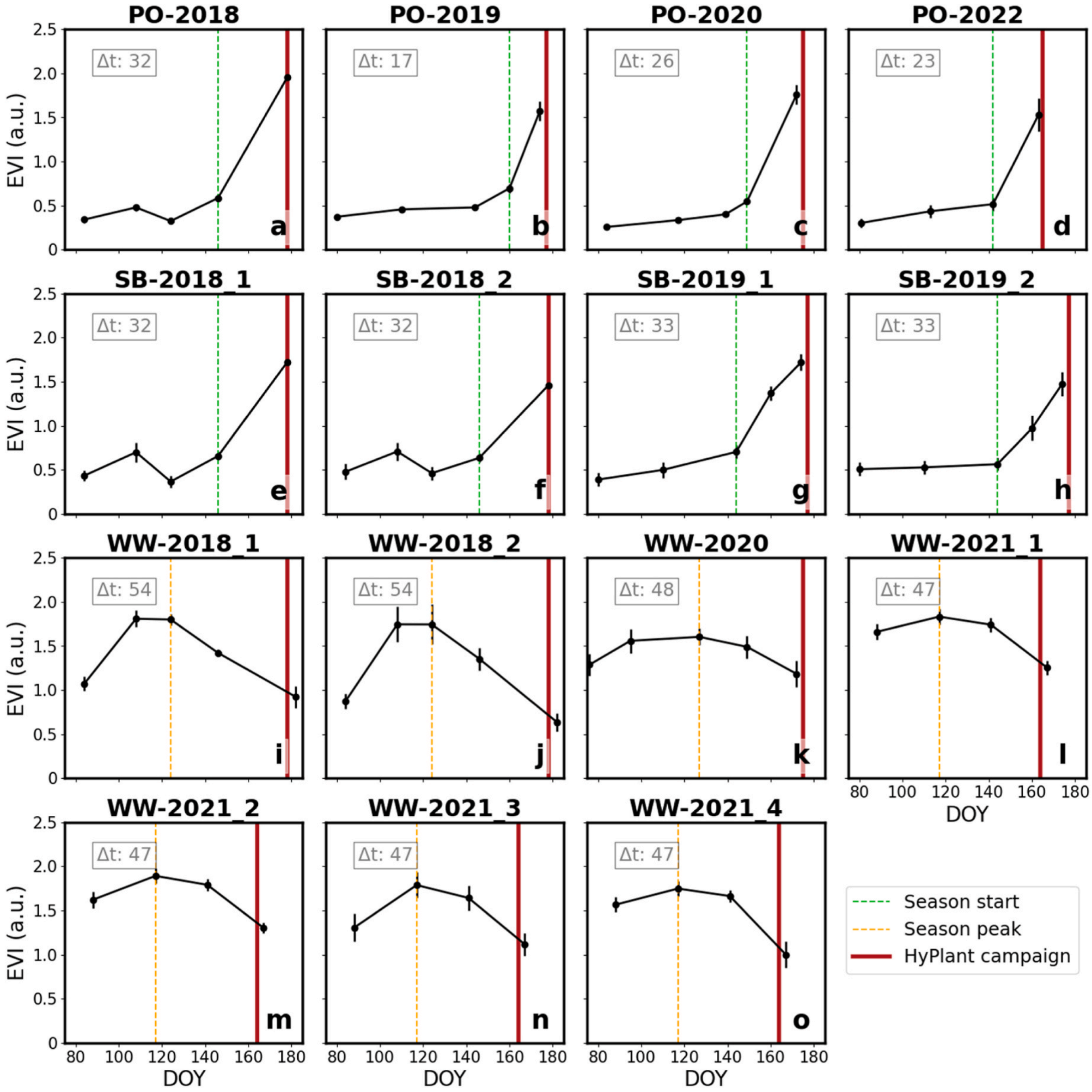

Fig. 5. Seasonal enhanced vegetation index (EVI) from nano-satellite information for each irrigated potato (PO; a-d), and rainfed sugar beet (SB; e-h) and winter wheat (WW; i-o) fields. Each data point represents the average and standard deviation of the EVI in the whole field. Green and yellow lines show the EVI increasing start and the EVI maximum as a reference of the start and peak of the growing season. The red line represents the date of the HyPlant airborne data collection. In text boxes, the elapsed time (Δt) between the start (for irrigated potato and rainfed sugar beet fields) and the peak (for rainfed winter wheat fields) of the growing season and the HyPlant data collection date are reported. DOY stands for "day of the year".

shoot growth (Zhou et al., 2018), and (iv) alterations in leaf morphology and physiology (Petrík et al., 2023). See Appendix 3 for a graphical overview. These physiological responses to variations in soil water availability in turn influence photosynthetic efficiency and canopy function (Liu et al., 2018), thereby modulating the emission of SIF (Shan et al., 2021). This is reflected in the different levels of SIF and eSIF observed across species (Figs. 4 and 7) where, consistent with Hou et al. (2023), the lower levels of SIF and eSIF occur in later growth stage crops like winter wheat, while the higher values are characteristic of early vegetative stages like potato and sugar beet. Complementing this observation, our PAW-LAI analysis (Fig. 8) in sugar beet shows that denser canopies (LAI >3) exhibit a more pronounced eSIF sensitivity to PAW variation.

Our results indicate that sugar-beet fields, known to present a strong stomatal closure response to soil limitations (Schickling et al., 2016), exhibited the strongest correlation between eSIF and PAW. This result can also be associated to the early phenological (actively growing; Hou et al., 2023) stage of this crop, when plants are more sensitive to even slight variations in water supply due to the combination of a high demand for water (FAO, 2012), and a shallow root system. In turn, in irrigated potato fields, the high SIF values characteristic of well-watered fields (Shan et al., 2021) lack of correlation with PAW indicating that the water needs of this crop were fully supplied by the farmers irrigation. According to Wu et al., 2024), in this condition, the SIF signal is expected to be mainly governed by factors other than soil moisture, such as PAR. As a result, SIF was solely dependent on the development of the crop as indicated by LAI and the corresponding greenness indices NDVI and EVI. Our wheat fields were mapped at the latest developmental stage where pigment breakdown, senescence and corn filling are the first order factors determining canopy reflectance. The reduction in total canopy chlorophyll characteristic of this phase was also primarily influencing top-of-canopy SIF, and therefore, no second order correlation between SIF and PAW was visible in wheat. Indeed, the non-existing SIF-PAW and the negative eSIF-PAW relations observed in winter wheat

Table 2

Phenology classification for each studied field, according to the elapsed time (Δt) between the start (for irrigated potato and rainfed sugar beet fields) and the peak (for rainfed winter wheat fields) of the growing season and the HyPlant data collection date. The start and peak of the growing season was identified based on the seasonal enhanced vegetation index (EVI) as shown in Fig. 5.

Crop	Field	Δt (days)	Phenology class
Irrigated potato	2018	32	Advanced_3
	2019	17	Early
	2020	26	Advanced_2
	2022	23	Advanced_1
Rainfed sugar beet	2018_1	32	Early
	2018_2	32	Early
	2019_1	33	Early
	2019_2	33	Early
Rainfed winter wheat	2018_1	54	Early
	2018_2	54	Early
	2020	48	Advanced
	2021_1	47	Advanced
	2021_2	47	Advanced
	2021_3	47	Advanced
	2021_4	47	Advanced

fields at advanced phenology, can be explained by the locally different ripening times. During this stage, chlorophyll breakdown (triggered to sustain the grain filling stage) already started producing spatial patterns that are independent from the short-term PAW heterogeneity.

Leaf-level reactions to water limitations, such as stomatal closure and reduction of the RuBisCo metabolic efficiency are strongly regulated. These adaptions occur within minutes, hours, and days to provide a well-balanced metabolism even in times with temporarily limited water supply. Such short-term reactions can be detected with SIF, as long as structural canopy effects can be compensated via reference areas (Damm et al., 2022) or as demonstrated here through the eSIF normalization. Thus, the significant positive eSIF-PAW correlation observed in sugar beet fields suggests the presence of a short-term physiological reaction of the sugar beet plants to momentarily limiting soil water availability. Considering the established conceptual model of van der Tol et al. (2014), it is safe to assume that sugar beet is operating in the middle domain, where SIF emission is determined by a regulated balance between photosynthetic electron use and non-photochemical energy dissipation (NPQ). As hypothesized, we found a significant positive eSIF–PAW relationship in the rainfed sugar-beet fields, consistent with De Cannière et al. (2022), who reported lower SIF emission yields in experimental plots where associated with reduced soil water content. In contrast, Wang et al. (2023) reported a weaker but existent response of eSIF to water stress. The authors attributed this to reduced SIF emissions resulting from increased NPQ, triggered to prevent leaf overheating when stomata close to avoid water loss. A similar regulatory mechanism may also explain the lower eSIF values measured in our study in soil units with reduced PAW.

Although our measurements were collected at one single time point, the knowledge provided on other studies that have analyzed the SIF dynamics across the day can help us to understand in more detail the eSIF-PAW correlation found in sugar beet fields. Since airborne data were collected at a time when SIF in sugar beet tends to increase (~10:30 h; Siegmann et al. (2021); Schickling et al. (2016)) alongside with photochemical activity (Pinto et al., 2016), the positive eSIF–PAW relationships might indicate greater photosynthetic rate (van der Tol et al., 2016) in soil units with higher PAW. This is supported by results of Schickling et al. (2016), who reported that SIF of sugar beet, but not of winter wheat, closely follows variations in the photosynthetic efficiency in the diurnal course. A similar positive SIF-PAW relation observed in the early phenology winter wheat field (Fig. 6c, dark red symbols) lost its significance after normalization to eSIF (Fig. 6f, dark red symbols), indicating that the initial SIF-PAW relationship was influenced by structural canopy effects that were corrected through the downscaling process. However, no relation was found in the late phenology winter wheat (Fig. 6f, orange symbols), suggesting that the dynamic leaf-level regulation may have affected the SIF signal at this advanced developmental stage, thus potentially leading to underestimations of the SIF-PAW relationship. This interpretation is consistent with Ruehr et al.

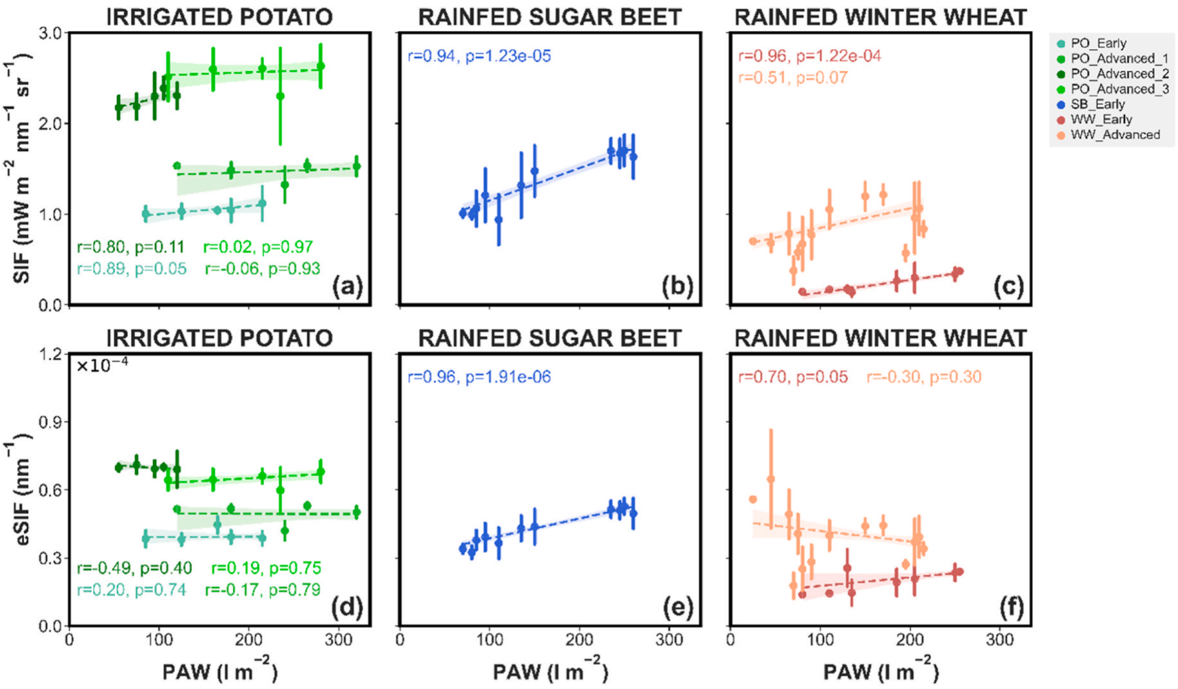

Fig. 6. Solar-induced chlorophyll fluorescence (SIF) and its emission efficiency at leaf-level (eSIF) plotted vs. the plant available water (PAW) for the irrigated potato (PO; a, d), and rainfed sugar beet (SB; b, e) and winter wheat (WW; c, f) fields. The color coding aims to differentiate data points belonging to different crops and phenological stages. Each data point represents the average and the standard deviation (bars) of all soil units under the same PAW level. Dashed lines represent linear regressions, and the corresponding Pearson correlation coefficients (*r*) and significance levels (*p*) are shown within each panel.

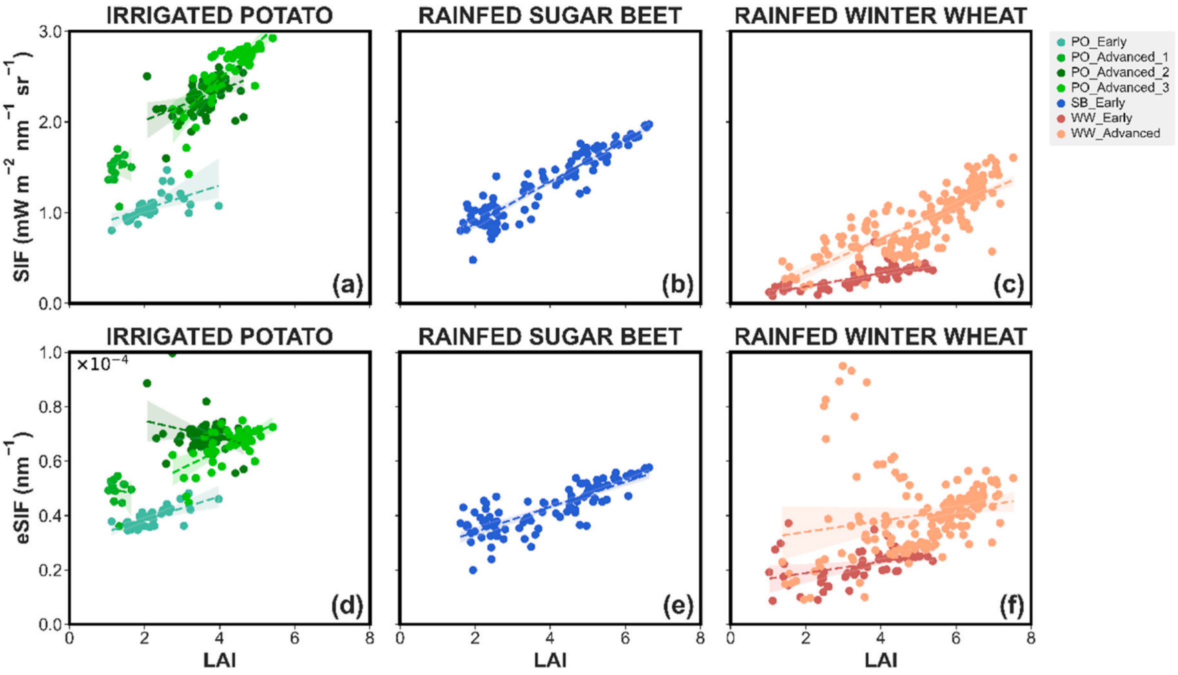

Fig. 7. Solar-induced chlorophyll fluorescence (SIF) and its emission efficiency at leaf-level (eSIF) plotted vs. the leaf area index (LAI) for the irrigated potato (a, d), rainfed sugar beet (b, e) and winter wheat (c, f) fields. The color coding differentiates data points belonging to different crops and phenological stages. Each data point represents the average and the standard deviation (bars) of all soil units under the same plant available water (PAW) level.

Table 3
Pearson coefficient (r) and its significance (p), alongside the relative slopes and residuals for linear regressions of Solar-induced chlorophyll fluorescence (SIF) and its emission efficiency at leaf-level (eSIF) with the leaf area index (LAI). RS and RMD stand for relative slope and relative mean deviation, respectively.

Crop	SIF				eSIF			
	r	*p*	RS (%)	RMD (%)	*r*	*p*	RS (%)	RMD (%)
PO_Early	0.56	<0.01	3.75	22.18	0.74	<0.01	4.31	29.80
PO_Advanced_1	0.16	0.55	4.22	37.05	−0.11	0.69	−3.15	53.39
PO_Advanced_2	0.46	<0.01	4.77	48.05	−0.28	0.02	−3.21	81.25
PO_Advanced_3	0.77	<0.01	11.11	26.33	0.64	<0.01	6.65	37.46
SB_Early	0.93	<0.01	6.58	12.01	0.81	<0.01	4.59	24.79
WW_Early	0.76	<0.01	2.09	1.46	0.41	<0.01	2.08	14.70
WW_Advanced	0.81	<0.01	5.26	4.37	0.20	<0.01	2.04	29.92

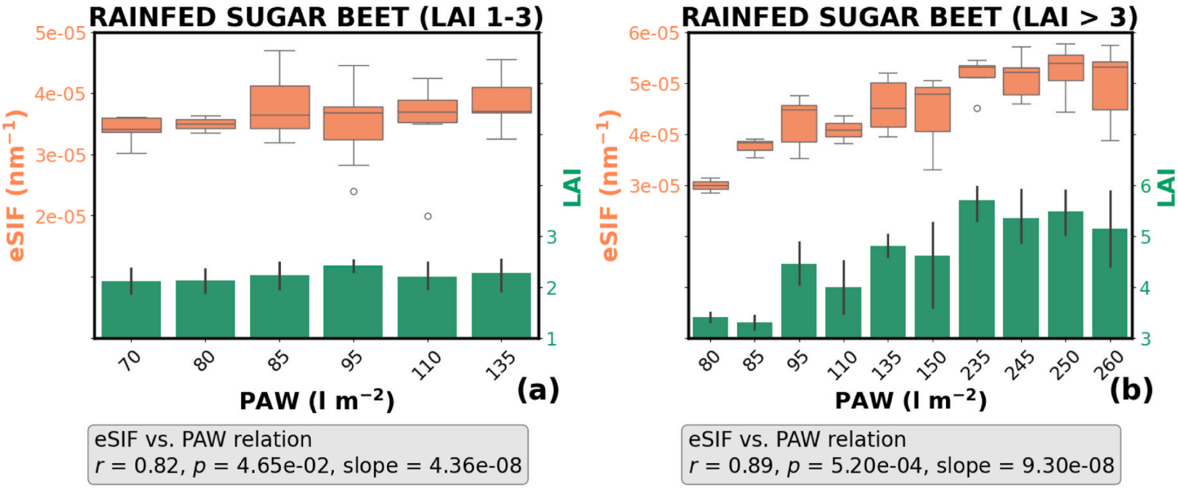

Fig. 8. Relation between the solar-induced chlorophyll fluorescence emission efficiency at leaf-level (eSIF) and the leaf area index (LAI) with the plant available water (PAW) in rainfed sugar beet fields at low (LAI 1–3; a) and high (LAI >3; b) canopy densities. Empirical statistics are summarized in the grey boxes.

(2024), who commented on how factors like progressing senescence

reduce the coupling between SIF and photosynthetic activity, thereby weakening the physiological link that underlines SIF responses to soil water availability.

Additional factors possibly affecting our findings of the SIF–PAW and eSIF-PAW relations include soil properties such as carbon content, nutrient status (especially N-content), and soil compaction. These soil properties can affect crop growth and, thus, determine spatial heterogeneity of SIF emissions. Irrespective of the influence of these soil properties, the soil profile depth is likely the most important factor in the study region, due to its heterogeneous geology and associated pedology (Rudolph et al., 2015). In general, the lowest PAW found in the investigated area is related to a shallow soil depth, and these areas also show lower SIF. It is important to note that a shorter soil profile will also impact other soil properties alongside PAW, with nutrient availability being the most relevant one. However, nutrient (especially N) shortage in the study area is unlikely to be the main reason, as farmers in the region typically apply high amounts of mineral fertilizers. Additionally, the soil organic carbon content was found to be relatively homogeneous across the study area (Reichenau et al., 2020).

4.2. *Methodological constraints*

The limitations of the empirical normalization of SIF to eSIF must be recognized, as it does not fully eliminate canopy-related factors. Even though the overall decrease of the correlation coefficient and the relative slopes in the eSIF-LAI correlations (compared with the SIF vs. LAI cases) indicate the functioning of the downscaling approach, we suspect that the NIRvH2 approach does not fully eliminate canopy related effects, but it largely reduces them. Additional information on the effect of the used downscaling method can be drawn from the residuals of the eSIF-PAW linear regressions (Table 3), in the sense that higher residuals values can indicate a stronger effect of the downscaling method. Remarkably, in rainfed sugar beet fields, the residuals in the eSIF-LAI relationship are twice as large as those in the SIF-LAI relationship. These findings, complemented with the reduced effect of LAI in the eSIF vs. PAW relationship observed in low density (LAI <3) canopies, indicates that these areas are more sensitive to limited (rainfed) water supply, and therefore more responsive to even slight PAW variations. Consequently, we consider that the eSIF variations under such environmental conditions describe the spatial variability of the photosynthetic activity in response to varying levels of water supply.

We investigated the eSIF-PAW relationship using single eSIF snapshots during evolving soil water fluctuations. Since the relationship between SIF and soil water content is highly dynamic through wet-dry transitions (Wu et al., 2024), a limitation of our study, is the lack of SIF and PAW information at higher temporal resolution to assess how their relationship vary during other times of the day and the growing season. Consequently, the strength of the eSIF-PAW correlation observed in the sugar been fields could potentially reflect a momentary linkage captured under specific environmental and phenological conditions. This motivates further research on a diurnal scale across the entire season to analyze, e.g., the relationship between SIF and PAW during the so-called midday depression, and during the afternoon recovery of photosynthesis at specific phenological stages.

Another limitation is, in the absence of more accurate soil water content information, the use of PAW information which relies on soil characteristics delineated by a geophysics-based soil map and by using a specific PTF. This strategy was made necessary by the extent of the investigated area, the required resolution, the estimation of PAW up to 2 m depth, and the inclusion of multiple years. It should also be noted that this soil map is currently the most accurate available representation for the Selhausen's soils and that the use of the Rawls and Brakensiek PTF in this area has been further validated in several studies (Brogi et al., 2020, Brogi et al., 2021; Jakobi, 2020; Guo et al., 2025). Nonetheless, using soil maps and PTFs can introduce uncertainties (Weihermüller et al., 2021), and further investigations should aim to use high-resolution soil moisture measurements, when possible, if the investigated patterns are highly dynamic. Within this context, recent advancements in remote sensing technology for soil moisture estimation, although limited to the topsoil, can be supportive. For instance, airborne radar technology like the scanning L-band active passive (SLAP) sensor operated by NASA (Kim, 2015), or the satellite-based soil moisture passive and active (SMAP) and SMOS (Ma et al., 2019) data sources of NASA and ESA, respectively, have great potential for comprehensive analysis alongside SIF information.

4.3. *Towards more comprehensive remote sensing-based assessments of crop responses to evolving water limitation*

Since soil water limitation provokes numerous different responses in plants acting at different temporal scales, its effect on the spectral properties of vegetation is different and might not only be related to the emission of SIF (Gerhards et al., 2019). Therefore, the complementary use of SIF- with thermal- and reflectance-based information is important to detect the cascade of physiological and structural changes undergone by plants under water stress conditions (Damm et al., 2018). Considering this, integrative multi-sensor approaches must be developed and employed for effective plant water stress monitoring (Berger et al., 2022; Panigada et al., 2014). It is worth mentioning that such complementarity among data sources should account for the severity of water limitation or even drought stress being analyzed, as well as the cascade of plant adaptation processes at different temporal scales. In this context, our findings demonstrate that SIF data enables the identification of functional plant adaptations to varying water availability.

Despite providing novel insights into the SIF-PAW relationship from unique datasets, further work is needed to develop more comprehensive SIF-based assessments of crop responses to varying PAW. Such efforts are essential to draw broadly applicable conclusions and to strengthen confidence in using eSIF as an indicator of plant-level water limitation. Analyses should encompass a wider range of environments, developmental stages, and species (Hu et al., 2025), complemented by complemented by in situ physiological observations of plant water status, e. g. those related to transpiration dynamics (Ahmed et al., 2023).

5. Conclusions

The relationship between eSIF and PAW varies across crop types and environmental gradients in terms of the interplay between environmental factors, seasonal growth patterns, and physiological processes. The downscaling approaches applied in this study can clearly help to enhance the contribution of leaf-level SIF on the measured canopy SIF signal and suppress the superimposing SIF dynamics caused by canopy structure. E.g., stress related regulation of young sugar-beet in response to water limitation can be clearly extracted from the eSIF signal, supporting the use of SIF as sensitive signal of vegetation stress. By identifying and understanding these spatial correlations, we can provide novel insights into the impact of varying levels of soil water content on the spatial distribution of eSIF. This new information is nowadays of utmost importance to advance our knowledge towards the development of SIF-based tools for early water stress detection, and thus for monitoring agricultural water management. Such advancements are crucial to address the growing food needs of humanity in the near future, when frequency and severity of drought events are expected to increase.

CRediT authorship contribution statement

Juan Quiros-Vargas: Writing – review & editing, Writing – original draft, Visualization, Methodology, Investigation, Formal analysis, Data curation, Conceptualization. **Cosimo Brogi:** Methodology, Formal analysis, Data curation, Conceptualization. **Alexander Damm:** Writing – review & editing, Supervision, Conceptualization. **Bastian Siegmann:** Writing – review & editing, Supervision, Conceptualization. **Patrick Rademske:** Software, Data curation. **Vicente Burchard-Levine:** Data

curation. **Vera Krieger:** Conceptualization. **Marius Schmidt:** Data curation. **Jan Hanuš:** Data curation. **Mauricio Martello:** Data curation. **Lutz Weihermüller:** Conceptualization. **Onno Muller:** Funding acquisition, Conceptualization. **Uwe Rascher:** Writing – review & editing, Supervision, Resources, Project administration, Funding acquisition, Conceptualization.

Declaration of competing interest

The authors declare the following financial interests/personal relationships which may be considered as potential competing interests: The authors confirm that there are no relevant affiliations, activities, financial involvements, or other relationships that could be perceived as influencing the integrity and objectivity of this research. If there are other authors, they declare that they have no known competing financial interests or personal relationships that could have appeared to influence the work reported in this paper.

Acknowledgments

The authors acknowledge funding from: (i) the Deutsche Forschungsgemeinschaft (DFG, German Research Foundation) – 491111487; (ii) the ESA's ‘PhotoProxy campaign’ project, under the contract no. 4000125731/19/NL/LF; (iii) ESA's FLEXSense campaign (ESA Contract No. 4000125402/18/NL/NA); and (iv) the European Union's (EU's) Training on Remote Sensing for Ecosystem Modeling (TRuStEE) consortium founded through the Horizon 2020 research and innovation program under the Marie Sklodowska-Curie grant agreement no. 721995. Support for data acquisition was provided by the SFB/TR 32 “Patterns in Soil–Vegetation–Atmosphere Systems: Monitoring, Modeling, and Data Assimilation” subproject D2 (www.tr32.de), funded by the Deutsche Forschungsgemeinschaft (DFG). We also thank the ‘Strukturwandel-Projekt Bioökonomie REVIER’ funded by the German Federal Ministry of Education and Research project (ID 031B0918A), the Deutsche Forschungsgemeinschaft (DFG, German Research Foundation) under Germany's Excellence Strategy – EXC 2070–390732324, and the support of the ATLAS project funded through the EU's Horizon 2020 research and innovation program under grant agreement No. 857125. The authors also appreciate valuable field measurement data acquired and shared by the HGF initiative TERestrial ENvironmental Observations (TERENO) and the ICOS project of the European Research Infrastructure programme (ESFRI). We acknowledge as well Prof. Dr. Sergio Cogliati for sharing the SFM code for the retrieval of SIF.

Appendix 1. **Extended version of Fig. 3 containing more details about the materials and methods used. This figure separates information according to inputs, processes, outputs, and analyses implemented with the airborne (a–c) and soil (d–h) datasets. The statistical analysis was done by overlapping the outputs from the remote sensing and soil data processing. All abbreviations are provided at the bottom of the figure**

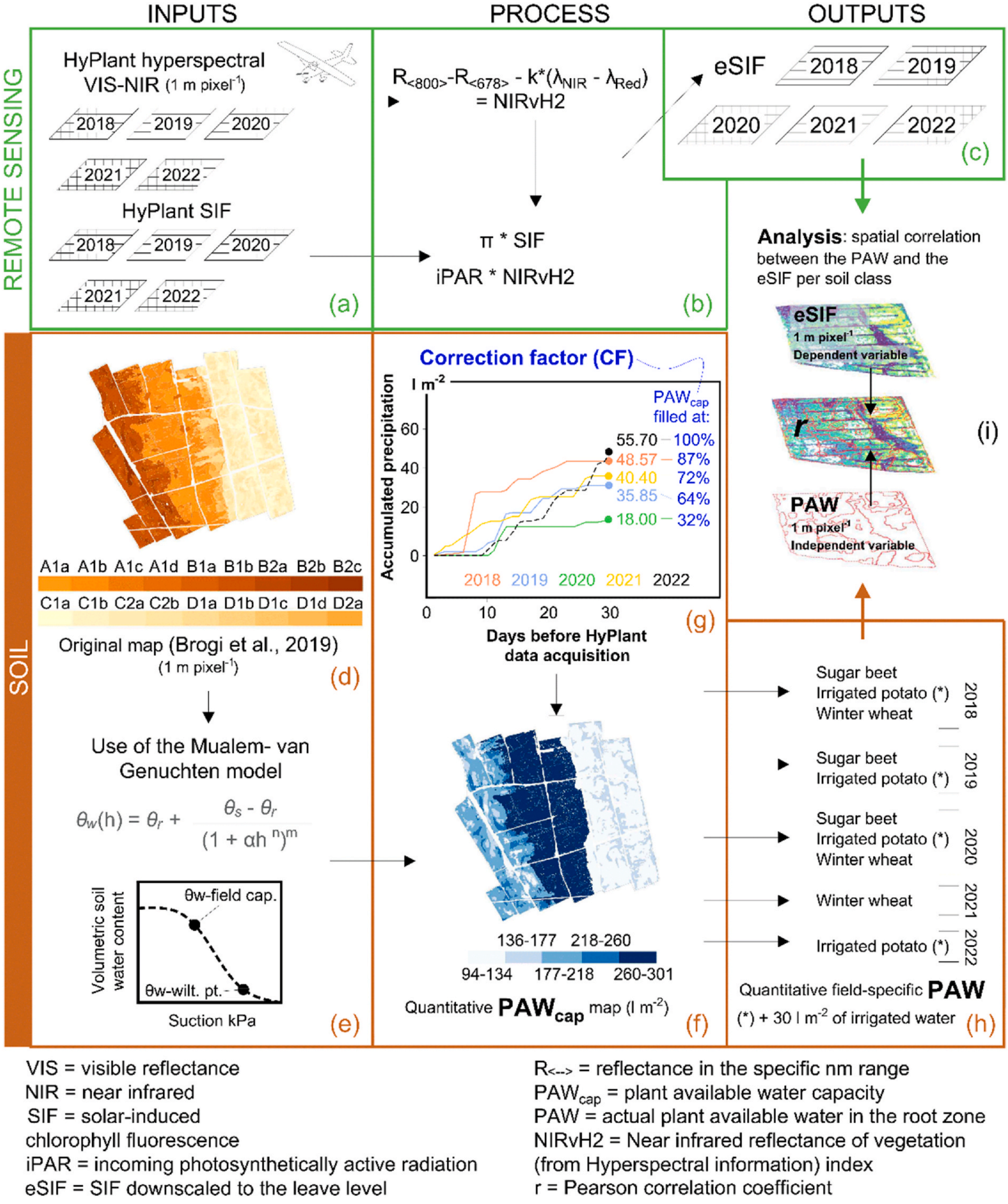

Appendix 2. Comparison between the plant available water capacity (PAW_{cap}) estimated with the methods used in the present manuscript (a), and 2130 soil moisture (SM) data points collected with a time-domain reflectometry (TDR)-based device at 5 cm depth (b). SM data were collected the same day of the high-performance airborne imaging spectrometer (HyPlant) campaign in 2019 (June 26th reported by Mengen et al. (2021)). The PAW_{cap} correlated with SM at $r = 0.99$ ($p < 0.01$; c). Background image: enhanced vegetation index (EVI) computed from HyPlant data June 27, 2018

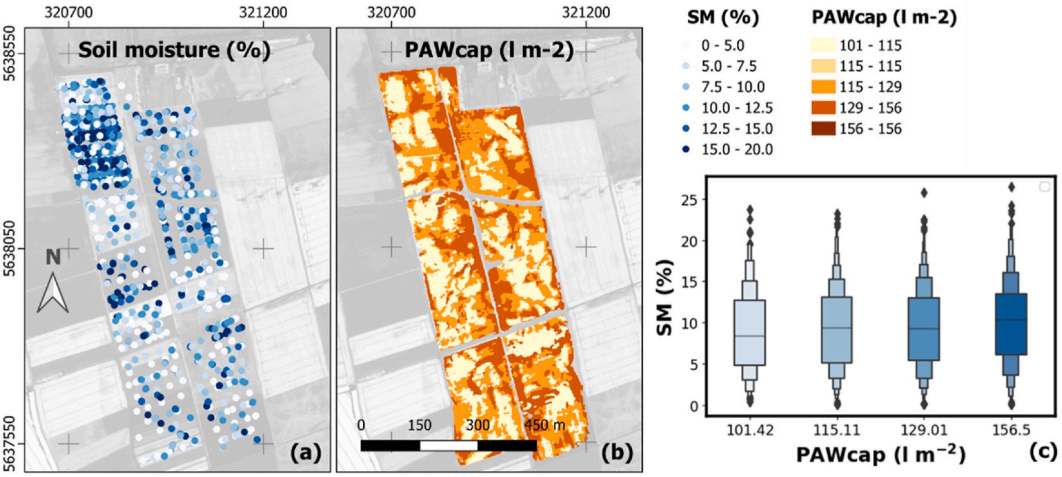

Appendix 3. Plant physiology- (a1) and soil-related (a2) factors that can confound the solar-induced chlorophyll fluorescence (SIF) plant-available water (PAW) relation due to their influence on the spatio-temporal expression of a stress detected in the SIF signal (b). Thick black lines indicate a link between the confounding factors and SIF. RGB image in panel (a2): True-color RGB composite derived from airborne HyPlant data acquired on June 27, 2018

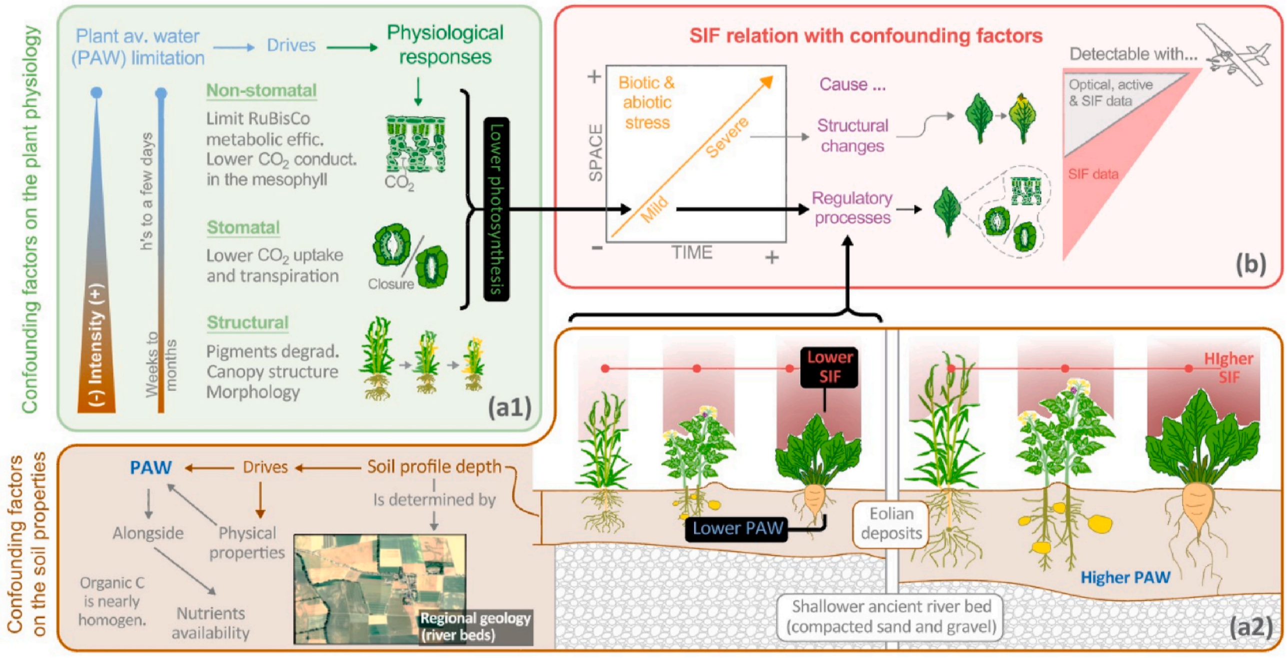

Data availability

The datasets generated and analyzed in this study are publicly available through the following link: https://doi.org/10.26165/JUELICH-DATA/WD5YUJ.

References

Abdalla, M., et al., 2022. Stomatal closure during water deficit is controlled by below-ground hydraulics. Ann. Bot. 129 (2), 161–170. https://doi.org/10.1093/aob/mcab141.

Ahmed, M., et al., 2023. Empirical insights on the use of sun-induced chlorophyll fluorescence to estimate short-term changes in crop transpiration under controlled water limitation. ISPRS J. Photogrammetry Remote Sens. 203, 71–85. https://doi.org/10.1016/j.isprsjprs.2023.07.016.

Badgley, G., Field, C.B., Berry, J.A., 2017. Canopy near-infrared reflectance andterrestrial photosynthesis. Sci. Adv. 3, e160224. https://www.science.org/doi/epdf/10.1126/sciadv.1602244?src=getftr.

Brakensiek, D., Rawls, W., 1994. Soil containing rock fragments: effects on infiltration. Catena 23, 99–110. https://doi.org/10.1016/0341-8162(94)90056-6.

Berger, K., et al., 2022. Multi-sensor synergies for crop stress detection and monitoring in the optical domain: a review. Remote Sens. Environ. 280, 113198. https://doi.org/10.1016/j.rse.2022.113198.

Brogi, C., et al., 2019. Large-scale soil mapping using multi-configuration EMI and supervised image classification. Geoderma 335, 133–148. https://doi.org/10.1016/j.geoderma.2018.08.001.

Brogi, C., et al., 2020. Simulation of spatial variability in crop leaf area index and yield using agroecosystem modeling and geophysics-based quantitative soil information. Vadose Zone J. 19, e20009. https://doi.org/10.1002/vzj2.20009.

Brogi, C., et al., 2021. Added value of geophysics-based soil mapping in agro-ecosystem simulations. SOIL 7, 125–143. https://doi.org/10.5194/soil-7-125-2021.

Christmann, A., et al., 2007. A hydraulic signal in root-to-shoot signalling of water shortage. TPJ 52 (1), 167–174. https://doi.org/10.1111/j.1365-313x.2007.03234.x.

Cogliati, S., et al., 2015. Retrieval of sun-induced fluorescence using advanced spectral fitting methods. Remote Sens. Environ. 169, 344–357. https://doi.org/10.1016/j.rse.2015.08.022.

Daddow, R.L., Warrington, G., 1983. Growth-Limiting Soil Bulk Densities as Influenced by Soil Texture. United States.

Damm, A., et al., 2018. Remote sensing of plant-water relations: an overview and future perspectives. J. Plant Physiol. 277, 3–19. https://doi.org/10.1016/j.jplph.2018.04.012.

Damm, A., et al., 2022. Response times of remote sensing measured sun-induced chlorophyll fluorescence, surface temperature and vegetation indices to evolving soil water limitation in a crop canopy. Remote Sens. Environ. 273, 112957. https://doi.org/10.1016/j.rse.2022.112957.

De Cannière, S., et al., 2022. Remote sensing of instantaneous water stress water stress at canopy level using sun-induced chlorophyll fluorescence and canopy reflectance. Remote Sens. 14, 2642. https://doi.org/10.3390/rs14112642.

Dietrich, D., 2018. Hydrotropism: how roots search for water. J. Exp. Bot. 69 (11), 2759–2771. https://doi.org/10.1093/jxb/ery034.

Drusch, M., et al., 2017. The FLuorescence EXplorer Mission Concept—ESA's Earth Explorer 8. IEEE Trans. Geosci. Rem. Sens. 55 (3), 1273–1284. https://doi.org/10.1109/TGRS.2016.2621820.

Food and Agricultural Organization of the United Nations (FAO), 2012. Crop yield response to water. https://www.fao.org/3/i2800e/i2800e.pdf. (Accessed 4 February 2022).

Gao, X., et al., 2000. Optical–biophysical relationships of vegetation spectra without background contamination. Remote Sens. Environ. 74, 609–620. https://doi.org/10.1016/S0034-4257(00)00150-4.

Gerhards, M., et al., 2019. Challenges and future perspectives of Multi-/Hyperspectral thermal infrared remote sensing for crop water-stress detection: a review. Remote Sens. 11 (10), 1240. https://doi.org/10.3390/rs11101240.

Guanter, L., et al., 2014. Global and time-resolved monitoring of crop photosynthesis with chlorophyll fluorescence. Proc. Natl. Acad. Sci. U.S.A 111 (14), E1327–E1333. https://doi.org/10.1073/pnas.1320008111.

Guo, X., et al., 2025. Enhancing carbon flux estimation in a crop growth model by integrating UAS-derived leaf area index. Agric. For. Meteorol. 374. https://doi.org/10.1016/j.agrformet.2025.110776.

Hu, C., et al., 2025. Specific responses to environmental factors cause discrepancy in the link between solar-induced chlorophyll fluorescence and transpiration in three plantations. Remote Sens. 17 (9), 1625. https://doi.org/10.3390/rs17091625.

Hou, J., et al., 2023. Identifying crop growth stages from solar-induced chlorophyll fluorescence data in maize and winter wheat from ground and satellite measurements. Remote Sens. 15 (24), 5689. https://doi.org/10.3390/rs15245689.

Huete, A., et al., 2002. Overview of the radiometric and biophysical performance of the MODIS vegetation indices. Remote Sens. Environ. 83, 195–213.

Jacquemoud, S., et al., 2009. PROSPECT+ SAIL models: a review of use for vegetation characterization. Remote Sens. Environ. 113, S56–S66. https://doi.org/10.1016/j.rse.2008.01.026.

Jakobi, J., 2020. Error estimation for soil moisture measurements with cosmic ray neutron sensing and implications for rover surveys. Frontiers in Water 2, 10. https://doi.org/10.3389/frwa.2020.00010.

Jonard, F., et al., 2020. Value of sun-induced chlorophyll fluorescence for quantifying hydrological states and fluxes: current status and challenges. Agric. For. Meteorol. 291, 108088. https://doi.org/10.1016/j.agrformet.2020.108088.

Kim, E., 2015. Scanning L-Band Active Passive (SLAP) – recent results from an airborne simulator for SMAP. In: Proceedings of the IEEE International Geoscience and Remote Sensing Symposium. IGARSS, Milan, Italy.

Krämer, J., Siegmann, B., et al., 2025. Downscaling the full-spectrum solar-induced fluorescence emission signal of a mixed crop canopy to the photosystem level using the hybrid approach. Remote Sens. Environ. 324, 114739. https://doi.org/10.1016/j.rse.2025.114739.

Liu, L., et al., 2018. Relationship of root zone soil moisture with solar-induced chlorophyll fluorescence and vegetation indices in winter wheat: a comparative study based on continuous ground-measurements. Ecol. Indic. 90, 9–17. https://doi.org/10.1016/j.ecolind.2018.02.048.

Liu, Z., et al., 2023. Diurnal pattern of sun-induced chlorophyll fluorescence as reliable indicators of crop water stress. IEEE Geoscience and Remote Sensing Letters (GRSL) 20, 2503805. https://doi.org/10.1109/LGRS.2023.3300149.

Ma, H., et al., 2019. Satellite surface soil moisture from SMAP, SMOS, AMSR2 and ESA CCI: a comprehensive assessment using global ground-based observations. Remote Sens. Environ. 231, 111215. https://doi.org/10.1016/j.rse.2019.111215.

Mengen, D., et al., 2021. The SARSense campaign: air- and space-borne C- and l-band SAR for the analysis of soil and plant parameters in agriculture. Remote Sens. 13, 825. https://doi.org/10.3390/rs13040825.

Meroni, M., et al., 2009. Remote sensing of solar-induced chlorophyll fluorescence: review of methods and applications. Remote Sens. Environ. 113 (10), 2037–2051. https://doi.org/10.1016/j.rse.2009.05.003.

Mohammadi, K., et al., 2022. Flash drought early warning based on the trajectory of solar-induced chlorophyll fluorescence. Proc. Natl. Acad. Sci. USA 119 (32), e2202767119. https://doi.org/10.1073/pnas.2202767119.

Mohammed, G.-H., et al., 2019. Remote sensing of solar-induced chlorophyll fluorescence (SIF) in vegetation: 50 years of progress. Remote Sens. Environ. 231, 111177. https://doi.org/10.1016/j.rse.2019.04.030.

Panigada, C., et al., 2014. Fluorescence, PRI and canopy temperature for water stress detection in cereal crops. Int. J. Appl. Earth Obs. Geoinf. 30, 167–178. https://doi.org/10.1016/j.jag.2014.02.002.

Patzold, S., et al., 2008. Soil heterogeneity at the field scale: a challenge for precision crop protection. Precis. Agric. 9, 367–390. https://doi.org/10.1007/s11119-008-9077-x.

Petrík, P., et al., 2023. Leaf physiological and morphological constraints of wateruse efficiency in C3 plants. AoB PLANTS 15, 1–14. https://doi.org/10.1093/aobpla/plad047.

Pinto, F., et al., 2016. Sun-induced chlorophyll fluorescence from high-resolution imaging spectroscopy data to quantify spatio-temporal patterns of photosynthetic function in crop canopies. Plant Cell Environ. 39, 1500–1512. https://doi.org/10.1111/pce.12710.

Planet Team, 2017. Planet application program interface: in space for life on Earth. https://www.planet.com/. (Accessed 1 May 2023).

Quiros, J., et al., 2020. Sun Induced Chlorophyll Fluorescence and Vegetation Indices for heat stress assessment in three crops at different geophysics-derived soil units. In: Proceedings of the American Geophysical Union. AGU, United States.

Ramachandran, P., et al., 2020. Coping with water limitation: hormones that modify plant root xylem development. Front. Plant Sci. 11, 570. https://doi.org/10.3389/fpls.2020.00570.

Rascher, U., et al., 2015. Sun-induced fluorescence – a new probe of photosynthesis: first maps from the imaging spectrometer HyPlant. Glob. Change Biol. 21 (12), 4673–4684. https://doi.org/10.1111/gcb.13017.

Rawls, W.J., Brakensiek, D., 1985. Prediction of soil water properties for hydrologic modeling. In: Jones, E.B., Ward, T.J. (Eds.), Watershed Management in the Eighties, pp. 293–299. United States.

Reichenau, T.G., et al., 2020. A comprehensive dataset of vegetation states, fluxes of matter and energy, weather, agricultural management, and soil properties from intensively monitored crop sites in western Germany. Earth Syst. Sci. Data 12, 2333–2364. https://doi.org/10.5194/essd-12-2333-2020.

Regaieg, O., et al., 2025. DART-based temporal and spatial retrievals of solar-induced chlorophyll fluorescence quantum efficiency from in-situ and airborne crop observations. Remote Sens. Environ. 319, 114636. https://doi.org/10.1016/j.rse.2025.114636.

Rudolph, S., et al., 2015. Linking satellite derived LAI patterns with subsoil heterogeneity using large-scale ground-based electromagnetic induction measurements. Geoderma 241–242, 262–271. https://doi.org/10.1016/j.geoderma.2014.11.015.

Ruehr, N.K., et al., 2024. Quantifying seasonal and diurnal cycles of solar-induced fluorescence with a novel hyperspectral imager. Geophys. Res. Lett. 51 (14). https://doi.org/10.1029/2023GL107429 e2023GL107429.

Schickling, A., et al., 2016. Combining sun-induced chlorophyll fluorescence and photochemical reflectance index improves diurnal modeling of gross primary productivity. Remote Sens. 8, 574. https://doi.org/10.3390/rs8070574.

Shan, X., et al., 2021. Structural and photosynthetic dynamics mediate the response of SIF to water stress in a potato crop. Remote Sens. Environ. 263, 112555. https://doi.org/10.1016/j.rse.2021.112555.

Shen, Q., et al., 2021. Relationship of surface soil moisture with solar-induced chlorophyll fluorescence and normalized difference vegetation index in different phenological stages: a case study of Northeast China. Environ. Res. Lett. 16, 024039. https://doi.org/10.1088/1748-9326/abd2f1.

Siegmann, B., et al., 2019. The high-performance airborne imaging spectrometer HyPlant—From raw images to top-of-canopy reflectance and fluorescence products: introduction of an automatized processing chain. Remote Sens. 11 (23), 2760. https://doi.org/10.3390/rs11232760.

Siegmann, B., et al., 2021. Downscaling of far-red solar-induced chlorophyll fluorescence of different crops from canopy to leaf-level using a diurnal data set acquired by the airborne imaging spectrometer HyPlant. Remote Sens. Environ. 264, 112609. https://doi.org/10.1016/j.rse.2021.112609.

Simmer, C., et al., 2015. Monitoring and modeling the terrestrial system from pores to catchments – the Transregional Collaborative Research Center on Patterns in the soil-vegetation-atmosphere system. Bull. Am. Meteorol. Soc. 96, 1765–1787. https://doi.org/10.1175/BAMS-D-13-00134.1.

Smola, A.J., Schölkopf, B., 2004. A tutorial on support vector regression. Stat. Comput. 14 (3), 199–222. https://doi.org/10.1023/B:STCO.0000035301.49549.88.

Sun, Y., et al., 2015. Drought onset mechanisms revealed by satellite solar-induced chlorophyll fluorescence: insights from two contrasting extreme events. Drought onset mechanisms revealed by satellite solar-induced chlorophyll fluorescence: insights from two contrasting extreme events. J. Geophys. Res.: Biogeosciences 120 (12), 2427–2440. https://doi.org/10.1002/2015JG003150.

Terrestrial Environmental Observations (TERENO), 2022. Data discovery portal. https://ddp.tereno.net/ddp/. (Accessed 3 January 2022).

van der Tol, C., et al., 2016. A model and measurement comparison of diurnal cycles of sun-inducedchlorophyll fluorescence of crops. Remote Sens. Environ. 186, 663–677. https://doi.org/10.1016/j.rse.2016.09.021.

van der Tol, C., et al., 2014. Models of fluorescence and photosynthesis for interpreting measurements of solar-induced chlorophyll fluorescence. JGR Biogeosciences 119, 2312–2327. https://doi.org/10.1002/2014JG002713.

van Genuchten, M.T., 1980. A closed-form equation for predicting the hydraulic conductivity of unsaturated soils. Soil Sci. Soc. Am. J. 44 (5), 892–898. https://doi.org/10.2136/sssaj1980.03615995004400050002x.

Verrelst, J., et al., 2019. Quantifying vegetation biophysical variables from imaging spectroscopy data: a review on retrieval methods. Surv. Geophys. 40, 589–629. https://doi.org/10.1007/s10712-018-9478-y.

von Hebel, C., et al., 2018. Understanding soil and plant interaction by combining ground-based quantitative electromagnetic induction and airborne hyperspectral data. Geophys. Res. Lett. 45, 7571–7579. https://doi.org/10.1029/2018GL078658.

Wang, N., et al., 2022. Potential of UAV-based sun-induced chlorophyll fluorescence to detect water stress in sugar beet. Agric. For. Meteorol. 323, 109033. https://doi.org/10.1016/j.agrformet.2022.109033.

Wang, N., et al., 2023. Decoupling physiological and non-physiological responses of sugar beet to water stress from sun-induced chlorophyll fluorescence. Remote Sens. Environ. 286, 113445. https://doi.org/10.1016/j.rse.2022.113445.

Wang, X., et al., 2022. Comparison of phenology estimated from monthly vegetation indices and solar-induced chlorophyll fluorescence in China. Front. Earth Sci. 10. https://doi.org/10.3389/feart.2022.802763.

Wantong, L., et al., 2023. Widespread and complex water stress effects on vegetation physiology inferred from space. Nat. Commun. 14, 4640. https://doi.org/10.1038/s41467-023-40226-9.

Weihermüller, L., et al., 2021. Choice of pedotransfer functions matters when simulating soil water balance fluxes. J. Adv. Model. Earth Syst. 13. https://doi.org/10.1029/2020MS002404 e2020MS002404.

Wu, Y., et al., 2024. Solar-induced chlorophyll fluorescence tracks canopy photosynthesis under dry conditions in a semi-arid grassland. Agric. For. Meteorol. 356, 110174. https://doi.org/10.1016/j.agrformet.2024.110174.

Xu, S., et al., 2018. Diurnal response of sun-induced fluorescence and PRI to water stress in maize using a near-surface remote sensing platform. Remote Sens. 10 (10), 1510. https://doi.org/10.3390/rs10101510.

Yang, P., et al., 2020. Fluorescence Correction Vegetation Index (FCVI): a physically based reflectance index to separate physiological and non-physiological information in far-red sun-induced chlorophyll fluorescence. Remote Sens. Environ. 240, 111676. https://doi.org/10.1016/j.rse.2020.111676.

Yang, P., van der Tol, C., 2018. Linking canopy scattering of far-red sun-induced chlorophyll fluorescence with reflectance. Remote Sens. Environ. 209, 456–467. https://doi.org/10.1016/j.rse.2018.02.029.

Yoshida, Y., et al., 2015. The 2010 Russian drought impact on satellite measurements of solar-induced chlorophyll fluorescence: insights from modeling and comparisons with parameters derived from satellite reflectances. Remote Sens. Environ. 166, 163–177. https://doi.org/10.1016/j.rse.2015.06.008.

Zeng, Y., et al., 2022. Combining near-infrared radiance of vegetation and fluorescence spectroscopy to detect effects of abiotic changes and stresses. Remote Sens. Environ. 270, 112856. https://doi.org/10.1016/j.rse.2021.112856.

Zeng, Y., et al., 2021. Estimating near-infrared reflectance of vegetation from hyperspectral data. Remote Sens. Environ. 267, 112723. https://doi.org/10.1016/j.rse.2021.112723.

Zeng, Y., et al., 2019. A practical approach for estimating the escape ratio of near-infrared solar-induced chlorophyll fluorescence. Remote Sens. Environ. 232, 111209. https://doi.org/10.1016/j.rse.2019.05.028.

Zhang, et al., 2023. Large diurnal compensatory effects mitigate the response of Amazonian forests to atmospheric warming and drying. Sci. Adv. 9, eabq4974.

Zhou, G., et al., 2018. Drought-induced changes in root biomass largely result from altered root morphological traits: evidence from a synthesis of global field trials. Plant Cell Environ. 41, 2589–2599. https://doi.org/10.1111/pce.13356.